Mon. Not. R. Astron. Soc. **000**, 000–000 (2013) Printed 12 March 2022 (MN LATEX style file v2.2)

A break in the high-redshift stellar mass Tully–Fisher relation ⋆

Lise Christensen† and Jens Hjorth
[1] *Dark Cosmology Centre, Niels Bohr Institute, University of Copenhagen, Juliane Maries Vej 30, 2100 Copenhagen, Denmark*

Accepted 2017 June 03. Received 2017 June 02; in original form 2016 January 17

ABSTRACT

We investigate the stellar-mass Tully–Fisher relation (TFR) between the stellar mass and the integrated gas velocity dispersion, quantified by the kinematic estimator $S_{0.5}$ measured from strong emission lines in spectra of galaxies at $0 < z < 5$. We combine luminosity-selected galaxies ('high-luminosity sample') with galaxies selected in other ways ('low-luminosity sample') to cover a range in stellar mass that spans almost five orders of magnitude: $7.0 \lesssim \log M_*/M_\odot \lesssim 11.5$. We find that the logarithmic power-law slope and normalisation of the TFR are independent of redshift out to $z \sim 3$. The scatter in the TFR is < 0.5 dex such that the gas velocity dispersion can be used as a proxy for the stellar mass of a galaxy independently of its redshift. At $z > 3$ the scatter increases and the existence of a correlation is not obvious. The high-luminosity sample exhibits a flatter slope of 1.5 ± 0.2 at $z < 3$ compared to the low-luminosity sample slope of 2.9 ± 0.3, suggesting a turnover in the TFR. The combined sample is well fit with a break in the TFR at a characteristic stellar mass scale of $M_* \sim 10^{10} M_\odot$, with no significant evolution out to $z \sim 3$. We demonstrate that a break in the TFR with a steeper slope at the low-mass end is a natural consequence of galaxy models with a mass-dependent stellar to halo-mass ratio.

Key words: galaxies: high-redshift – galaxies: fundamental parameters – galaxies: kinematics and dynamics – galaxies: evolution

1 INTRODUCTION

Scaling relations for galaxies can provide insight into their formation and evolution, with the caveat that sometimes the relations depend strongly on selection effects. Disk galaxies are known to follow the Tully–Fisher relation (TFR) (Tully & Fisher 1977), for which the luminosity L correlates with the maximum disk rotational velocity $L \propto V^{3.5}$. The power-law slope depends somewhat on the adopted photometric band. While the traditional TFR studies of rotational velocity versus luminosity include galaxies with regular disk morphologies, investigations have also shown that both early- and late type galaxies follow the same TFR in the local universe (Trujillo-Gomez et al. 2011; Cortese et al. 2014). As the luminosity of a galaxy is roughly proportional to its total stellar mass, there is also a stellar-mass TFR. Compared to the luminosity based TFR, local galaxies have a steeper stellar-mass TFR (independent of photometric band) with $M_* \propto V^{4.3}$ (Bell & de Jong 2001).

Several investigations have examined the evolution of the stellar-mass TFR with redshift (see Glazebrook 2013, for a comprehensive review), and although sample sizes are small at higher redshifts, observations have revealed that the TFR slope and normalisation is constant to $z \sim 1.5$ (Milvang-Jensen et al. 2003; Conselice et al. 2005; Flores et al. 2006; Miller et al. 2011, 2012). A small scatter in the TFR is obtained only when selecting ordered disk galaxies without complex morphologies (Flores et al. 2006; Puech et al. 2008). Other studies report redshift evolution of the TFR with a change in normalisation of 0.3–0.5 dex towards lower mass at a given velocity between $z \sim 0.6$ and $z \sim 2$ (Puech et al. 2008; Cresci et al. 2009; Vergani et al. 2012), and at $z = 3$ a change in the TFR normalisation downwards by 1 dex has been reported, albeit with a large uncertainty (Gnerucci et al. 2011).

Aside from the small samples sizes involved in studying the high-redshift TFR, one caveat is that the dynamical range of galaxy masses is limited since spectroscopic observations have primarily pre-selected the brighter and more massive galaxies (e.g. Erb et al. 2006b; Förster Schreiber et al. 2009; Contini et al. 2012). This necessitates assuming a constant TFR slope in determining the TFR relation. The issue of redshift evolution of the TFR (or lack thereof) therefore remains unsettled (Miller et al. 2012).

The two quantities that are primarily used to study galaxy disk kinematics are the rotation velocity $V_{\rm rot}$ and the velocity dispersion, σ. Velocity dispersions can be difficult to derive in high-redshift quiescent galaxies, but it is easily measured from emission-line widths in star-forming galaxies. At high redshifts, galaxies have higher ratios of velocity dispersion to rotation ve-

⋆ Based on data from the X-shooter GTO observations collected at the European Southern Observatory VLT/Kuyuen telescope, Paranal, Chile, under programme IDs: 084.B-0351(D), 086.A-0674(A), 086.A-0674(B), 087.A-0432(A) and 087.A-0432(B).

† Email: lise@dark-cosmology.dk

locity (Genzel et al. 2006; Förster Schreiber et al. 2009), revealing complex dynamics and reflecting that disks are not yet settled. Whereas high-spatial resolution adaptive optics observations coupled with integral field spectroscopy can disentangle the rotation and dispersion components, it is important to recall that such investigations primarily target some of the most massive, and hence luminous, galaxies at these redshifts. Obtaining the same level of detailed kinematics in large samples of low-mass high-redshift galaxies is not yet technically feasible.

To address these shortcomings, a variant of the classic TFR involving a combination of the velocity dispersion and the rotation velocity (Weiner et al. 2006),

$$S_K = \sqrt{KV_{\rm rot}^2 + \sigma^2}, \quad (1)$$

better represents the depths of the potential wells of galaxies that are either dispersion or rotation dominated, or unsettled disks that are common at higher redshifts. Using this combination with $K = 0.5$, Kassin et al. (2007) found a smaller scatter compared to the classic TFR for galaxies at $z \lesssim 1.2$, although Miller et al. (2011) found no improvement by including a rotational component in the relation. Using data from the SAMI- integral field data survey of 235 nearby galaxies, Cortese et al. (2014) reported a tight M_*–$S_{0.5}$ relation for both gas and stellar components in galaxies of any Hubble type. Extending the analysis with literature data on massive galaxies at higher redshifts, including a few up to $z = 3.8$, Kassin et al. (2012) did not find any indications of redshift evolution of the TFR, although they did find that the relation between the rotation velocity and velocity dispersion does change with redshift.

The classic TFR has a small scatter when choosing galaxies with well-ordered disks and smooth rotation curves. Including galaxies with a range of morphologies and luminosities cause a larger scatter, which may increase at higher redshifts as galaxies have increasing disordered rotations. The aim of this paper is to investigate the $M_* - S_{0.5}$ relation for a wide selection of galaxies reported in the literature. Rather that trying to build a complete sample of luminosity-selected galaxies that by far dominate the sample papers in the literature, we here explore if galaxies selected through alternative methods show a similar relation and scatter as luminosity-selected galaxy samples. In addition to luminosity-selected samples we therefore include galaxies that are selected independently of their intrinsic luminosities and hence probe the lower-mass and lower-luminosity end of the distribution. Taking advantage of strong gravitational lensing, and deeper observations on faint galaxies, we study galaxies in a wide dynamical range of almost five orders of magnitude in stellar mass from $7 \lesssim \log M_* \lesssim 12$, and extend the TFR to $z \sim 5$. In Section 2 we describe the data set, and explore the linear- and non-linear TFR in Sections 3 and Section 4. We briefly investigate relations for the star-formation rates in Section 5. Section 6 discusses the findings and compares with other investigations, and Sect. 7 presents the summary.

2 DATA SETS

As the stellar mass TFR has been well studied at $z \lesssim 1$ using luminosity selected samples (Weiner et al. 2006; Kassin et al. 2007, 2012; Cortese et al. 2014), this paper primarily focuses on collecting higher redshift samples. We compile stellar masses and integrated velocity dispersions from the literature, and, when available, we also compile the inferred rotational velocities ($V_{\rm rot}$). Although the primary goal is to investigate galaxies at $z > 1$, we also include a local sample of 16 galaxies at $z \sim 0.2$ that are analogues to high-redshift Lyman break galaxies (Gonçalves et al. 2010) in order to establish a low-redshift baseline for comparison to the high-redshift galaxy samples.

With the advent of effective spectrographs on large telescopes, the kinematics of hundreds of galaxies at $z \sim 2$ have now been studied. To date, by far the largest number of well-studied galaxies at $z \sim 1 - 3$ are relatively massive luminosity-selected ones (Pettini et al. 2001; Erb et al. 2006a; Förster Schreiber et al. 2009; Cresci et al. 2009; Law et al. 2009; Wright et al. 2009; Pérez-Montero et al. 2009; Lemoine-Busserolle & Lamareille 2010; Lemoine-Busserolle et al. 2010; Gnerucci et al. 2011; Swinbank et al. 2012; Queyrel et al. 2012; Contini et al. 2012; Epinat et al. 2012; Lehnert et al. 2013; Kulas et al. 2013; Steidel et al. 2014; Wisnioski et al. 2015). Some individual galaxies appear in several papers. We avoid including the same galaxy twice. AO observations combined with integral field data have been used to analyse spatially resolved kinematics of galaxies, rather than a single measurement of their integrated velocity dispersions (Förster Schreiber et al. 2009; Gnerucci et al. 2011; Epinat et al. 2012). Integral field spectra are vital to recover the maximum rotation velocity of the galaxies, because slit-orientations may not follow exactly the rotational axis of the galaxies. Roughly half of the galaxies in the luminosity-selected samples included in this paper are observed with integral-field spectral data, where galaxy inclinations can be measured, and the inferred rotational velocities include the modelled inclinations. Moreover, integral field spectra can reveal variations in the measured velocity dispersion across the galaxies. For resolved spectroscopic measurements we adopt the reported integrated or average velocity dispersions. When only the line FWHM are reported, we assume that the line has a Gaussian line profile and σ = FWHM/2.35.

To examine a large dynamical range in galaxy masses, we need data from low-mass galaxies at higher redshifts. The main limitation is that in order to resolve the emission lines and derive the intrinsic velocity dispersions, which are of the order of a few tens of km s^{-1}, a resolving power of $R > 5000 - 10000$ is needed. Low-mass, faint high-redshift galaxies observed at intermediate resolution will have spectra with lower signal-to-noise ratios, and the samples sizes are consequently limited. The galaxy luminosity function at $z > 2$ has a steep slope at the low-luminosity end, but these low-mass galaxies are rarely targeted specifically for follow-up spectroscopy except in special circumstances that use different selection methods.

Taking advantage of strong gravitational lensing by foreground clusters of galaxies is a way to mitigate the problem of low S/N ratio data, and several lensed galaxies have recently been observed at a sufficiently high spectral resolution to allow the derivation of the velocity dispersion. In this paper we use data for 44 lensed galaxies at $1 < z < 5$ complied from the literature (Teplitz et al. 2000; Siana et al. 2008; Swinbank et al. 2009; Hainline et al. 2009; Bian et al. 2010; Pettini et al. 2010; Christensen et al. 2010; Jones et al. 2010; Richard et al. 2011; Wuyts et al. 2012a; Christensen et al. 2012b,a; Wuyts et al. 2012b; Yuan et al. 2012; Jones et al. 2013; Belli et al. 2013), again avoiding duplications.

Other selection methods also probe preferentially the low-mass end of the galaxy mass function. These include the host galaxies of explosive events such as gamma-ray bursts (GRBs) or supernovae (SNe). We include 39 mostly low stellar-mass galax-

ies that hosted GRBs and which have measured stellar masses[1] (Savaglio et al. 2009; Perley et al. 2013; Krühler et al. 2015). Although the total number of well-investigated GRB hosts is more than 100, few are observed at sufficiently high spectral resolution to allow a measurement of the intrinsic velocity dispersion. For a few host galaxies, σ or the FWHM of emission lines are not reported, and we retrieved and analysed ESO/X-shooter archive data in these cases. Original values presented in various papers on GRB host galaxies are summarised in Table A1.

Because of the limited sample sizes, we also include galaxies selected using other methods, such as two host galaxies of Type Ia SNe at $z \sim 1.5$ (Frederiksen et al. 2012, 2014), and a host galaxy of a super-luminous SN (Leloudas et al. 2015), nine Lyα emission selected galaxies (Rhoads et al. 2014), three DLA galaxies (Péroux et al. 2011; Fynbo et al. 2013; Krogager et al. 2013), and finally 14 extreme emission line galaxies (Maseda et al. 2013).

The rotational velocity component for these non-luminosity-selected galaxies is rarely measured and reported along with the velocity dispersion. One of the limiting factors is the spatial resolution which prohibits the determination of the rotational velocity. Fortunately, galaxies at high redshifts are increasingly dominated by their intrinsic velocity dispersions (Genzel et al. 2006; Förster Schreiber et al. 2009). Moreover, for spatially unresolved galaxies, the one-dimensional spectra provide an integrated velocity dispersion which includes a rotational component due to beam smearing. It can be shown that both dispersion dominated galaxies and galaxies with pure rotation, viewed edge on, have a line width of $S_{0.5}$ (Rhoads et al. 2014). Therefore, $S_{0.5}$ is measured irrespectively of whether the galaxy is dominated by ordered or random motions.

The stellar masses reported in the literature and which we use in this paper are based on conventional spectral energy distribution (SED) fitting techniques, which find the best match among a set of galaxy spectral template models to broad-band photometric data points. Deriving stellar masses for galaxies above $z \sim 3$ depend critically on the availability of infra-red photometry without which stellar masses might be underestimated. The luminosity-selected galaxy sample is observed with Spitzer, while that is not the case for all other selections. This will cause an increased scatter of the measurements at the very highest redshifts. One of the dependent parameters in SED fits is the stellar initial mass function (IMF) used in creating galaxy spectral templates. Authors typically either use a Salpeter (Salpeter 1955) or a Chabrier IMF (Chabrier 2003). When necessary, we convert the reported total stellar masses to a Chabrier IMF by dividing the mass inferred using a Salpeter IMF by a factor of 1.8. When reported, we also compile the star-formation rates (SFRs) of the galaxies, again corrected to a Chabrier IMF. Different diagnostics are used to infer the galaxies SFRs, e.g. [OII], Hα, or UV luminosities. As these trace the SFRs on different time scales but mostly agree within a factor of $\sim$2, the compiled values have an increased scatter. Additionally, some stellar masses and SFRs are reported adopting different cosmologies, and we convert the reported stellar masses to that that of a flat cosmology with $H_0 = 70$ km s^{-1} Mpc^{-1} and $\Omega_\Lambda = 0.73$.

To summarise, the sample of galaxies can be split according to two distinct selection methods: Galaxies that are selected via their luminosities and colours, or via properties less directly related to their brightness, namely lensed galaxies, DLA hosts, Lyα emitters, GRB and SN hosts, and extreme emission line galaxies.

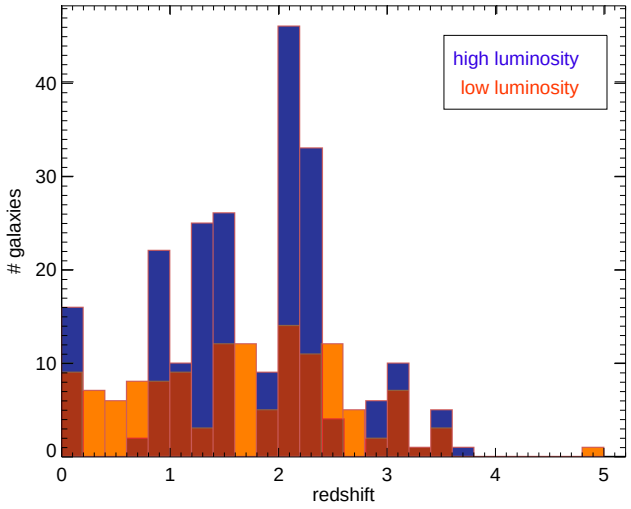

Figure 1. Redshift distributions of the high- and low-luminosity samples. The high-luminosity sample consists of 214 luminosity selected galaxies. The low-luminosity sample consists of 113 galaxies selected using alternative methods, such as gravitationally lensed galaxies, GRB-, SNe-, DLA-host galaxies, Lyα emitters and extreme emission line galaxies.

Broadly, the two samples comprise high-luminosity galaxies and low-luminosity galaxies, respectively. Although there is some overlap in luminosities between the two samples, the terminology we adopt here is to refer to them as the 'high-luminosity' and 'low-luminosity' galaxies. The combined sample consists of 327 galaxies at redshifts $0 < z < 5$, 214 of which are in the high-luminosity sample and 113 in the low-luminosity sample. The redshift distributions illustrated in Fig. 1 reveal that luminosity selection preferentially targets galaxies at specific redshift intervals where Hα falls in the H and K bands, causing conspicuous peaks around $z \sim 1.4$ and at $z \sim 2.2$, respectively. Conversely, the low-luminosity sample does not exhibit any clear overdensities in redshift space.

We compare our compilation to $\sim$200,000 star-forming galaxies from SDSS-DR9 tabulated in the MPA–JHU database[2]. Emission-line velocity dispersions are determined from the integrated spectrum within the 3 arcsec SDSS fibres (Thomas et al. 2013), and are corrected for instrument resolution (Tremonti et al. 2004). Rotational velocities are not reported for SDSS galaxies, but since velocity dispersions are measured within the central 3 arcsec fibre aperture, beam smearing of any rotational component will also contribute to the $S_{0.5}$ parameter. Stellar velocity dispersions based on SDSS spectra are commonly used to measure dynamical masses. Emission-line velocity dispersions are less frequently used for the same purpose, but is has been shown that in star-forming SDSS galaxies the ratio between the two measurements is close to 1 (Chen et al. 2008). We select star-forming galaxies with well-detected emission lines and emission-line ratios (according to the BPT diagram in Baldwin et al. 1981), and with velocity dispersions derived from forbidden emission lines. The reported stellar masses are based on a Kroupa IMF and are therefore corrected down by a factor of 1.06 to convert to a Chabrier IMF. We choose only galaxies with well-determined values of the velocity dispersion ($\sigma_{\rm SDSS}$) i.e., measurements with a signal-to-noise ratio >3.

[1] http://www.grbhosts.org/

[2] The SDSS catalogue data is obtained from http://www.sdss3.org/dr9/algorithms/galaxy_mpa_jhu.php

3 SCALING RELATIONS FOR STAR FORMING GALAXIES

In this section we explore how selections of galaxy samples influence the stellar mass TFR and its evolution with redshift.

3.1 Stellar mass Tully–Fisher relation

Using the combination of rotation and velocity dispersion in Equation 1 with $K = 0.5$ for galaxies at $z \lesssim 1.2$, Kassin et al. (2007) found a smaller scatter than when examining the TFR based only on the velocity dispersion (i.e., $K = 0$ in Eq. 1). We adopt $K = 0.5$ for the primarily high-mass, luminosity-selected galaxies that have a measurement of $V_{\rm rot}$, while for the remaining galaxies the reported velocity dispersions are representative for the $S_{0.5}$ parameter. $V_{\rm rot}$ is reported for half of the galaxies in the high-luminosity sample through measurements from IFU data. However, the analysis and results reported below are consistent if we investigate correlations with the velocity dispersion (σ) alone. Few of the galaxies have a much higher rotational component compared to their velocity dispersions, and with median values of σ= 82 km^{-1} and $S_{0.5}$=111 km s^{-1} for the samples with IFU data, the fits do not change. The intrinsic scatter of the relations do however increase by 50% for the samples at $z < 2.2$.

Figure 2 shows the TFR for all the galaxies in our compilation. The sample up to $z \sim 3$ has been split into three redshift bins with roughly equal numbers of galaxies in each bin. We fit the TFR with a linear function (in log space) taking into account the measurement uncertainties for the stellar masses and velocities. Where these errors are not reported, we assume a representative uncertainty of $\pm$0.2 dex in stellar mass (43 cases), and $\pm$0.1 dex in log $S_{0.5}$ (33 cases). To determine the slope and normalisation we use the LINMIX ERR IDL code (Kelly 2007), which employs a Bayesian approach and a Marcov chain Monte Carlo algorithm for the linear regression. It accounts for all measurement errors and includes an intrinsic scatter term. LINMIX ERR assumes symmetric error bars so we symmetrised all uncertainties (in log space). We choose LINMIX ERR because it is widely used and tested to examine for example the linear relation between black hole masses and velocity dispersions, is more robust to outliers.

Specifically, we fit a linear relation

$$\log M_* = A(\log S_{0.5} - 2.0) + B \pm \epsilon, \qquad (2)$$

where ϵ represents an intrinsic scatter of the relation. The subtracted value 2.0 is chosen because the slope and intercepts are strongly correlated, and it presents a value close to the median value $\log\ S_{0.5} = 1.93$ of all galaxies. A fit to all galaxies irrespective of their redshift gives $\log M_* = (2.40 \pm 0.15) \times \log S_{0.5} + (5.25 \pm 0.29)$ with a scatter of $\epsilon = 0.50$ dex in $\log M_*$. In comparison, Kassin et al. (2007) find a slope of 2.94 ± 0.38, a normalisation of 5.56 ± 0.82, and a scatter of $\epsilon = 0.47$ dex in M_* for all their galaxies at $0.1 < z < 1.2$.

Another linear chi-square minimising routine like FITEXY (Press et al. 1992) which includes both uncertainties of $S_{0.5}$ and M_*, with its modification to include an intrinsic scatter, MPFITEXY (Williams et al. 2010), gives the best fit $\log M_* = (2.45 \pm 0.14) \times \log S_{0.5} + (5.14 \pm 0.25)$ with a scatter of 0.49 dex in $\log M_*$, consistent with the results from LINMIX ERR.

3.2 Redshift evolution

To explore the evolution of the TFR with redshift, we divide the sample into four redshift bins. Table 1 shows a compilation of the best fit parameters and the number of galaxies in each redshift bin. Dividing the sample into high- and low-luminosity galaxies, the best fit parameters are listed in Table 1 and illustrated in the middle and bottom rows in Figure 2. At progressively higher redshifts, the lower detection limit of both velocity dispersions and the stellar masses increase. This is a selection effect since the least massive galaxies, which are also the least luminous ones, are not observed at sufficient spectral resolution.

Within each sub-sample, there is no strong evidence for redshift evolution at $z < 3$. The best fit logarithmic slopes, A, are depicted in Fig. 3 (since the best fit slopes and normalisations are highly correlated, an illustration of the normalisation would be similar). However, there are differences in the slopes of the two sub-samples. The low-luminosity galaxies have a steeper slope in any redshift bin at $z < 3$ with a slope of 2.9 ± 0.3 versus a slope of 1.5 ± 0.2 for the high-luminosity sample. When reversing the dependent and independent variables for the fits, we find the same trend of a flatter slope (for the inverse relation) of the low-luminosity relative to the high-luminosity sample at $z < 2.2$, a similar slope for the $2.2 < z < 3.0$ bin, and no relation for the highest redshift bin. The steepening of the slope seen in Fig. 2 is therefore not caused by a paucity of low-mass galaxies in the high-luminosity sample.

Previous investigations have analysed the change of the TFR normalisation with redshift for small samples while fixing the slope of the relation to a well-calibrated lower-redshift relation (e.g. Cresci et al. 2009; Gnerucci et al. 2011; Vergani et al. 2012). For consistency we examine the result of keeping the slope fixed to that of the full sample. We find no change in the best fit normalisation within 1-σ uncertainties between all the redshift bins, again suggesting that there is no redshift evolution. The TFR for galaxies at $z < 1.2$ in Kassin et al. (2007) is consistent with that from our combined sample in the low-redshift interval in Table 1.

Expanding equation 2 to include a redshift term, we find

$$\begin{aligned}\log M_* =& (2.37 \pm 0.14)[\log S_{0.5} - 2.0] + (10.00 \pm 0.28) \\ & (-0.1 \pm 0.2) \log(1+z).\end{aligned} \qquad (3)$$

The last term, $(-0.1 \pm 0.2) \log(1+z)$, minimises the scatter by a negligible 0.002 dex and does not justify including a redshift dependence. Fitting only galaxies that are not luminosity selected, the best fit for the redshift evolution term is $(-0.1 \pm 0.1) \log(1+z)$. We conclude that there is no evidence for significant redshift evolution of the TFR up to $z \sim 3$.

A linear fit to the individual SDSS galaxies in Fig. 2 above a resolution limit of $\log \sigma_{\rm SDSS} > 1.8$ gives $\log M_* = (2.34 \pm 0.09) \times (\log S_{0.5} - 2.0) + (10.57 \pm 0.01) \pm 0.28$. The slope is similar to that of the low-redshift sub-sample including all the galaxies in Table 1, within the 1σ uncertainty range. The difference in normalisation between the SDSS and the sample containing all galaxies at $z < 1.4$ is 0.52 ± 0.19, suggesting a moderate redshift evolution. The change in normalisation between the low-luminosity sample at $z < 1.4$ and the SDSS galaxies is smaller 0.31 ± 0.15. One reason for these different normalisations is that the shape of the distribution of SDSS galaxies does not appear to be linear, as we shall return to in Sect. 4.

Since $V_{\rm rot}$ is not measured for all the galaxies in the sample, and only very few galaxies in the low-luminosity sample have this value reported, it could affect the slope of the relation. Instead of

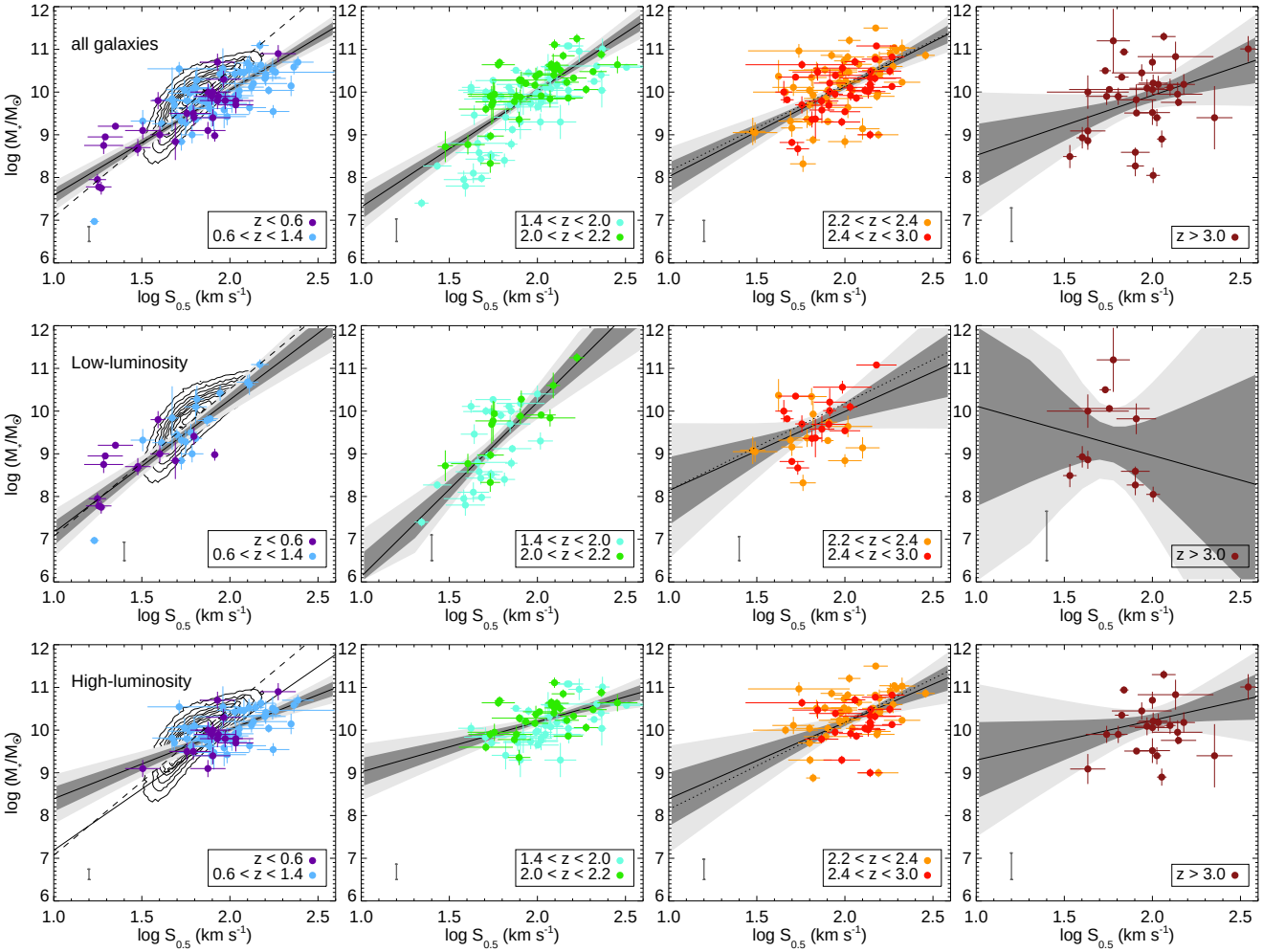

Figure 2. Stellar mass TFR in different redshift bins. All stellar masses are rescaled to those obtained with a Chabrier IMF (Chabrier 2003). The top row of panels show all galaxies in this study, the middle row the low-luminosity galaxies, and the bottom row the high-luminosity galaxies. The contours in the first column represent star-forming SDSS galaxies. The dashed line in the first column shows the relation derived from luminosity-selected $z \sim 1$ galaxies (Kassin et al. 2007), and the dotted line in the third column refers to galaxies at $z > 2$ (Barro et al. 2014). The linear fits are obtained with the LINMIX ERR code (Kelly 2007), and slopes and normalisations are reported in Table 1. The grey shaded regions represent 1- and 2σ confidence intervals respectively. Data points in the first three columns are colour coded in smaller redshift bins for visualisation purposes. The bar in the lower left corner in each panel represents the intrinsic scatter of the relation, and explains why galaxies fall outside the shaded confidence regions.

using $S_{0.5}$ we replace with the velocity dispersion, σ in all sub-samples and recompute the linear fits. Only in the high-luminosity sub-sample at $z < 1.4$ do the parameters change by more than 1σ uncertainties, giving a smaller slope compared to Table 1. One data set that contributes to the $z < 1.4$ bin has a significantly higher $V_{\rm rot}$ compared to σ (Gonçalves et al. 2010), and this drives the slope of the $M_* - \sigma$ relation to a flatter value. Accordingly, we conclude that using $S_{0.5}$ or σ does not change the overall results significantly.

4 A BREAK IN THE $M_* - \sigma$ RELATION

In the previous section we found that the slope of the TFR depends on the luminosity range considered, with a more shallow slope for luminous galaxies (Figs. 2 and 3). We here quantify the existence of a break in the TFR and discuss a possible interpretation.

4.1 Asymptotic $M_* - \sigma$ relation

To visualise the break in the relation we bin all galaxies in $S_{0.5}$ (16 galaxies in each bin) and compute the median in each bin (red filled circles in Fig. 4). This procedure implicitly assumes that there is no redshift evolution as suggested by our findings in the previous section. The uncertainty in the median is calculated by bootstrapping. Fig. 4 suggests that the turnover depends significantly on the lowest mass bin, which is primarily composed of $1.4 < z < 2$ galaxies from the low-luminosity sample (see Fig. 2, second column). Twelve of the 16 galaxies in the lowest mass bin have been observed at intermediate- to high spectral resolutions ($R > 6000$), and their emission lines are reported to be clearly resolved. If we exclude the other 4 galaxies observed at lower spectral resolutions ($R \sim 3000$), the lowest-mass bin still reveals a break from a linear relation.

Assuming that this apparent break in the $M_* - S_{0.5}$ relation is not a reflection of some unknown selection bias, we proceed to

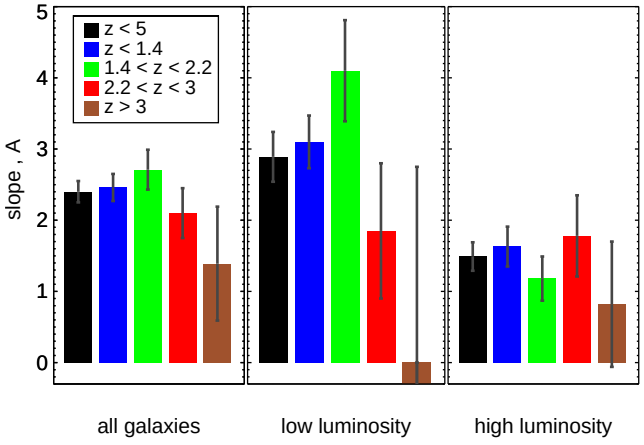

Figure 3. Best fitting linear logarithmic slopes (A) in Table 1 are shown for the subsamples containing all galaxies, low- and high-luminosity galaxies.

Table 1. Linear fits for the $M_* - S_{0.5}$ relation in Eq. 2. ϵ is the intrinsic scatter, ρ is the linear correlation coefficient for the data, and n is the number of galaxies in each bin. The last column gives the covariance between the slope and intercepts. The top five rows fit all the galaxies, the middle five rows represent fits to low-luminosity galaxies, while the bottom five rows include the high-luminosity galaxies only.

Sample	n	A	B	ϵ (dex)	ρ	cov.
All galaxies						
$0.0 < z < 5.0$	327	2.40±0.15	10.05±0.03	0.50	0.73	0.001
$z < 1.4$	96	2.46±0.19	10.05±0.05	0.35	0.87	0.005
$1.4 < z < 2.2$	106	2.73±0.28	10.01±0.06	0.54	0.76	0.004
$2.2 < z < 3.0$	91	2.11±0.35	10.13±0.06	0.49	0.64	0.0004
$z > 3.0$	34	1.42±0.76	9.93±0.15	0.79	0.39	0.044
Low luminosity						
$0.0 < z < 5.0$	113	2.87±0.35	10.06±0.11	0.61	0.69	0.03
$z < 1.4$	32	3.10±0.37	10.26±0.15	0.43	0.90	0.04
$1.4 < z < 2.2$	40	3.99±0.72	10.15±0.20	0.62	0.77	0.12
$2.2 < z < 3.0$	30	1.86±0.96	9.99±0.21	0.57	0.48	−0.08
$z > 3.0$	11	−1.29±3.00	8.95±0.83	1.15	−0.24	2.14
High luminosity						
$0.0 < z < 5.0$	214	1.49±0.21	10.13±0.03	0.41	0.53	−0.002
$z < 1.4$	64	1.63±0.30	10.02±0.05	0.25	0.76	0.0003
$1.4 < z < 2.2$	66	1.18±0.31	10.19±0.05	0.36	0.52	−0.087
$2.2 < z < 3.0$	61	1.79±0.58	10.18±0.08	0.48	0.49	−0.026
$z > 3.0$	23	0.81±0.89	10.10±0.14	0.62	0.28	−0.002

explore a model composed of a low-luminosity power law and a high-luminosity asymptotic (i.e., constant) limit,

$$\log M_* = \log M_{\rm lim} - \log\left[1 + \left(\frac{S_{0.5,\rm TO}}{S_{0.5}}\right)^{\gamma}\right], \qquad (4)$$

where $M_{\rm lim}$ is the asymptotic limiting mass, $S_{0.5,\rm TO}$ is the turnover value, and γ is the power-law slope at the low $S_{0.5}$ end. The fitting is done by χ^2 minimisation in IDL (using the unbinned data), and the best fit is shown as the solid red curve in the left panel of Fig. 4, with best fit values reported in Table 2. The low-mass end slope around $\gamma \sim 2.5$ is similar to best fit slopes for all galaxies in Section 3. γ asymptotes to A in the power-law (low-mass) limit.

Introducing more parameters in a model to produce a better fit of the stellar mass TFR can be justified. Including the intrinsic scatter (ϵ in Equation 2) serves to make the reduced χ^2 for the fit equal to 1. To evaluate if the asymptotic model provides a better fit than the linear model, we compute the Bayesian information criterion:

$$\mathrm{BIC} = n \ln\left(\sum_{i=1}^{n}(M_{*,i} - \hat{M}_i)^2/n\right) + k\ln(n),$$

where k is the number of parameters in the fit, n is the sample size, M_* is the measured stellar mass, and $\hat{M}_i$ is the expectation value from the model. For the binned sample, this gives BIC = –55 for the linear fit, and BIC = –62 for the asymptotic fit, and $\Delta(\mathrm{BIC}) = 7$ demonstrates a strong preference for the latter model.

Table 2. Asymptotic parameter fits to Eq. 4.

Sample	$\log M_{\rm lim}$ [$\log \mathrm{M}_\odot$]	$\log S_{0.5,TO}$ [km s^{-1}]	γ	scatter dex
SDSS	10.96±0.01	2.01±0.01	4.19±0.01	0.35
this sample	10.88±0.02	2.21±0.01	2.52±0.04	0.57

The grey scale area in Fig. 4 shows that SDSS galaxies display a turnover at high velocity dispersions, where the stellar mass approaches an asymptotic value. SDSS spectra have a resolution of $R \sim 2000$ corresponding to a velocity dispersion of 64 km s^{-1}. As $\sigma_{\rm SDSS}$ is corrected for instrument resolution, some line width measurements are very close to the instrument resolution and should be treated with caution. Emission lines with widths close to the instrumental resolution will have higher relative uncertainties of their widths, and choosing only very strong emission lines that satisfy the S/N criteria may skew the values towards higher σ at low stellar masses. If we impose a limit $\log\sigma_{\rm SDSS} > 1.6$, we find a turnover point at $\log\sigma_{\rm SDSS,TO} = 2.0$ (see Table 2), while a higher limit that represents the SDSS velocity resolution of $\log\sigma_{\rm SDSS} > 1.8$ gives a turnover point at $\log\sigma_{\rm SDSS,TO} = 2.05 \pm 0.01$, a shallower low-mass slope $\gamma = 3.20 \pm 0.04$ and a similar limiting mass $\log(M_{\rm lim}/\mathrm{M}_\odot) = 11.09 \pm 0.01$.

Aperture effects in the SDSS spectra may also play a role for galaxies with radii larger than the SDSS fiber size (e.g Brinchmann et al. 2004; Kewley et al. 2005). Imposing an additional criterion that the 90 percentage Petrosian radius is smaller than 1.5 arcsec leaves sample of just 235 SDSS galaxies. A fit to this small sample gives a larger turnover point $\log\sigma_{\rm SDSS,TO} = 2.20 \pm 0.06$, a low-mass slope $\gamma = 3.59 \pm 0.18$ and the same limiting mass $\log(M_{\rm lim}/\mathrm{M}_\odot) = 11.03 \pm 0.13$. As a turnover in the relation remains clear, we conclude that aperture effects do not impose a strong effect on the determination of σ. This is supported by the finding that emission line widths and gas velocity dispersions do not display large changes with radius in SDSS galaxies observed with integral field spectrographs (e.g. Gerssen et al. 2012; García-Lorenzo et al. 2015).

4.2 Simple model with a non-linear relation

The dynamics of a galaxy is governed by its total mass, and we can use this information to predict the velocity dispersion for a galaxy with a given mass. Simple equations lead to a scaling between the halo mass and its virial velocity dispersion $M_{\rm halo} \propto \sigma_v^3$ (Posti et al. 2014).

Models that match the dark-matter halo distribution with an observed galaxy mass distribution predict that the stellar mass to dark matter halo mass fraction depends on the halo mass. The stellar mass at the maximum fraction is around 10^{12} $\mathrm{M}_\odot$ at low redshifts (Guo et al. 2010), and this stellar mass increases with redshift

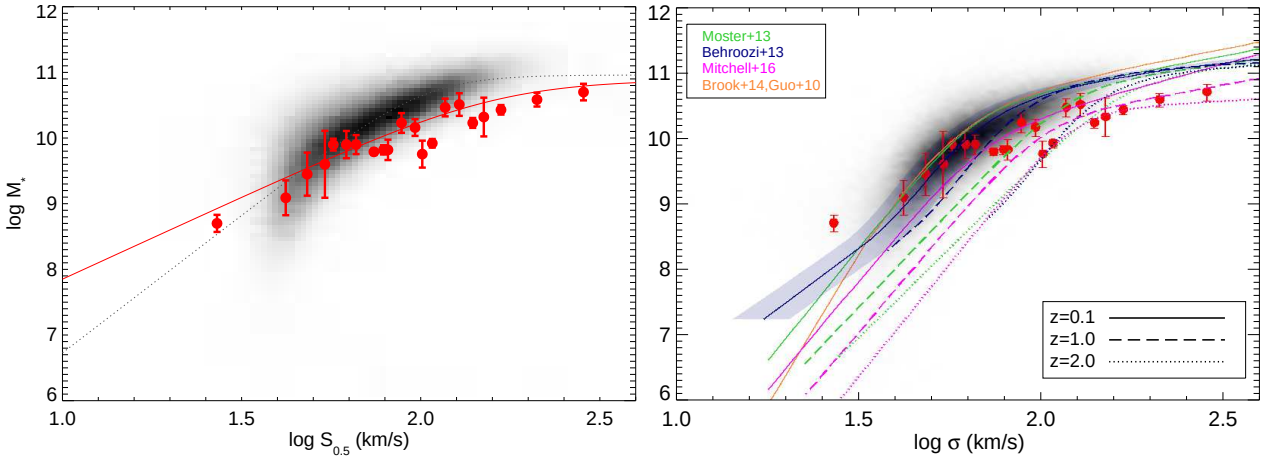

Figure 4. A non-linear relation of the stellar-mass TFR. The galaxies in our compilation are separated into bins with equal number of galaxies in each bin (red circles). The error bars are calculated by bootstrapping the median masses in each bin. The solid curve in the *left panel* represents a fit to Eq. 4 using unbinned data. The grey scale distribution represent ∼200,000 SDSS star-forming galaxies and the dotted curve is a fit to these. The fitting parameters suggests a similar asymptotic limit, while the turnover point for SDSS galaxies has a smaller velocity. *Right panel:* The halo-mass to stellar mass fraction models (Guo et al. 2010; Moster et al. 2013; Behroozi et al. 2013; Brook et al. 2014; Mitchell et al. 2016) combined with equations in Section 4.2 reproduce well the SDSS gas velocity dispersions at $z \sim 0.1$. The shaded blue region is the 68% confidence interval for the low redshift model from Behroozi et al. (2013). At higher redshifts, the models do not reproduce the observed data well, but a consistent fit can be obtained by changing the virial coefficient, C, to a higher value. In addition, a smaller stellar to total baryonic mass fraction at high redshift whould shift the data points downwards relative to the model predictions.

(Behroozi et al. 2013; Moster et al. 2013; Mitchell et al. 2016). The standard definition of the halo mass within a radius r is

$$M_{\rm halo} = \frac{4}{3}\pi r^3 \Delta_c(z)\rho_c(z), \quad (5)$$

where the halo mass is typically defined within the virial radius of the halo, Δ_c is the overdensity, and ρ_c, is the critical energy density in a flat universe $\rho_c(z) = \frac{3H(z)^2}{8\pi G}$ at redshift z. The Hubble parameter evolves as $H(z) = H_0 E(z)$ with $E(z)^2 = \Omega_{0,m}(1+z)^3 + \Omega_{0,\Lambda}$ when the radiation energy density can be neglected. The overdensity can be parametrised as

$$\Delta_c(z) = 18\pi^2 + 82[\Omega(z) - 1] - 39[\Omega(z) - 1]^2 \quad (6)$$

(Bryan & Norman 1998; Posti et al. 2014), where

$$\Omega(z) = \Omega_{0,m}(1+z)^3/E(z)^2. \quad (7)$$

In this parametrisation the overdensity at $z = 0$ is $\Delta_c(0) = 100$ and it increases with redshift.

The halo mass within a radius r can be computed from the velocity dispersion: $M_{\rm halo}(< r) = C\sigma_v^2 r/G$, where the virial coefficient C depends on the mass distribution within the halo, including also velocity anisotropies and any assumptions of a spherical or disk-like morphology of a galaxy. For an isothermal sphere, $C = 2$. C reflects the dominant contribution of the dark matter to the halo mass, whereas in observations of galaxies it primarily reflects galaxy properties measured within a typical ∼10 kpc radius, where the baryons also contribute to the mass. When deriving galaxy dynamical masses, values of $C = 5$ for r measuring the stellar half-light radius (e.g. Pettini et al. 2001; Shapley et al. 2004), or $C = 3.4$ appropriate for galaxies with disk-like morphologies (Erb et al. 2006b) have been chosen. Because C depends on mass distribution and galaxy morphology it will cause a scatter when deriving masses for a mixed galaxy sample when set to a single value.

Since we do not know the exact contribution of the halo mass within each galaxy and within the regions probed by the emission lines, we therefore take the approach that C is not known, but is likely to be in the range of 1–10.

Combining the above equations yields

$$M_{\rm halo} = \frac{\sqrt{2}\sigma_v^3}{G}\frac{C^{3/2}}{H(z)\Delta_c(z)^{1/2}}, \quad (8)$$

i.e., $M_{\rm halo}$ scales as σ_v^3 and the proportionality factor depends on the virial coefficient and redshift through $\sqrt{C^3/\Delta_c(z)}/H(z)$.

Halo masses are converted into stellar masses using models of stellar-to-halo mass fractions, and Equation 8 produces a prediction for the relation between M_* and σ_v. The right panel in Fig. 4 shows the binned data with overlayed halo-models (Moster et al. 2013; Behroozi et al. 2013; Mitchell et al. 2016) at redshifts $z = 0.1$, 1 and 2. The model in Brook et al. (2014) that describes low-mass halos is normalised to the higher-mass halo models in Guo et al. (2010). All models naturally have a break in the TFR due to the peak in the stellar-to-halo mass fraction around $M_{\rm halo} = 10^{12}$ M$_\odot$ (see also Fig. 6 in Guo et al. 2010). Halo abundance matching and computations of the rotational velocities also exhibit a steepening below ∼100 km s^{-1} (Trujillo-Gomez et al. 2011), and reproduce the observed velocity-luminosity relation galaxies with various morphologies including dwarfs, disk and giant elliptical galaxies.

The exact point of the break location depends on $\Delta_c, C, H(z)$ and the chosen halo models which vary with redshifts. The low-redshift models fit the SDSS data well for a choice of $C \approx 2.5$. In particular, the break in the relation and its normalisation are reproduced. Since the horizontal location of the models depend on the choice of C and Δ_c, other combinations could also provide a reasonable agreement. At higher redshifts however, some models fail and predict too high stellar masses for a given velocity dispersion, and the observed break is less pronounced than suggested by

Table 3. Linear relation fits for a SFR$-\sigma$ relation similar to Eq. 2.

Sample	n	A'	B'	ϵ' (dex)	ρ
$0 < z < 5$	308	2.05±0.17	1.42±0.04	0.57	0.62
$z < 1.4$	95	2.55±0.27	1.29±0.07	0.53	0.77
$1.4 < z < 2.2$	94	1.36±0.33	1.42±0.06	0.59	0.46
$2.2 < z < 3$	87	1.43±0.35	1.52±0.06	0.50	0.48
$z > 3$	32	1.97±0.63	1.64±0.13	0.64	0.58

the models. Decreasing the stellar-to-halo mass ratio by 0.3 dex would improve the normalisation of the fits, and the break points of the relations can shift to lower values of σ for a larger value of C. To reproduce the turnover point in the data, we determine that $C \approx 3-4$ and $C \approx 6-7$ at $z = 1$ and $z = 2$, respectively. The models illustrated in Fig. 4 all use a redshift invariant $C = 2.5$.

The average redshift of all the galaxies is $z = 1.9$ and most are selected by their star-formation properties in some form. Since they have a higher SFR relative to galaxies in the local universe (see Fig. 5), it is expected that they also have higher gas-fractions, which could shift their location downwards in Fig. 4. Deriving the stellar-to-halo mass ratio based on semi-analytic models that include gas consumption and conversion into stars results in a shift in normalisation with redshift (Mitchell et al. 2016), and which reproduces better the observations at the high-mass end. Low mass galaxies, on the other hand, should also have a downward shift in normalisation because of a higher gas fraction, but this shift is not seen in the data.

Although the simplistic approach to derive velocity dispersions based on halo models do not reproduce perfectly the data at $z > 1$, our conclusion is that the existence of a break in the relation can naturally be explained by a change in the stellar-to-dark-matter fraction with galaxy mass. Furthermore, the models also predict a shift of the turnover point towards higher velocity dispersions with redshift consistent with the 0.2 dex change from local galaxies to $z \sim 2$ galaxies listed in Table 2.

5 STAR-FORMATION RATE VERSUS $S_{0.5}$

Other scaling relations involving the velocity dispersion have been investigated. For example, Hβ luminosities of local- and high-redshift galaxies are found to be correlated with the widths of the lines (Melnick et al. 2000). Spatially resolved observations of galaxies at high redshifts also reveal that individual star-forming clumps have velocity dispersions which scale with their luminosities approximately as $L \propto \sigma^4$ (Wisnioski et al. 2012). Since Hβ luminosities scale linearly with the SFRs after correcting for internal extinction, a correlation with the SFR must exist as well.

The integrated gas velocity dispersions could be affected by star-formation and supernova feedback, in which case we would expect to see a strong σ–SFR correlation. Lehnert et al. (2013) analysed 53 galaxies at $z = 1$–3 observed with the VLT/Sinfoni integral field spectrograph and concluded that σ is driven by the SFR surface density. For 95 GRB hosts galaxies, i.e., non-luminosity selected galaxies, Krühler et al. (2015) investigated the σ-SFR relation and found a strong correlation with a linear slope of ∼4. They also reported marginal evidence (at the 1.5σ level) for a redshift evolution of the normalisation, assuming a fixed slope.

We fit all the galaxies with reported SFRs and $S_{0.5}$ to a linear relation in Fig. 5 with a best fit of: $\log M_* = (2.05 \pm 0.17) \times (\log S_{0.5} - 2.0) + (1.42 \pm 0.04)$ with an intrinsic scatter of 0.57 dex. As in Section 3, we separate galaxies into redshift bins and report the fits in Table 3. In all redshift bins the intrinsic scatter, ϵ, is larger than in the $M_* - S_{0.5}$ fits. Using the velocity dispersions, σ instead of the $S_{0.5}$ parameter does not change the scatter of the relation.

Compared to the results of Krühler et al. (2015), we derive a flatter slope at all redshifts, but if we fix the slope to that obtained for the full sample, the normalisation changes by 0.4 dex from the $z < 1$ to the $z > 3$ sub-samples. This change can be compared with the M_*–SFR relation where a ~ 0.5 dex increase in SFR from $z < 1$ to $z > 2$ for a given stellar mass has been inferred (Whitaker et al. 2014). Whereas the intercepts in Table 3 are consistent within 1σ uncertainties, the location of the 200,000 low-redshift star-forming SDSS galaxies is clearly shifted to lower SFRs in Fig. 5. The change in normalisation of the SFR-$S_{0.5}$ relation between SDSS galaxies and the high-luminosity- and low-luminosity samples is 0.3 and 0.6 dex, respectively. Since the M_*–$S_{0.5}$ relation appears constant with redshift out to $z \sim 3$, the reason for a varying SFR–σ likely reflects the observed mass-SFR scaling relation which is known to be redshift dependent (Noeske et al. 2007; Daddi et al. 2007), as the redshift change in the SFR-$S_{0.5}$ relation is similar to that seen in the mass-SFR scaling relation (Whitaker et al. 2014).

6 DISCUSSION

The existence of a relation between the stellar mass and emission line velocity dispersion parameter $S_{0.5}$ and its redshift evolution has been frequently analysed in the literature. By combining various galaxy samples and selection methods we have analysed the TFR covering a large redshift span out to $z \sim 5$. In this section we discuss how various effects influence the results and compare with previous studies.

6.1 Sample selection

Splitting up the galaxy samples into galaxies found in galaxy surveys and flux-limited samples, and galaxies that are found via alternative methods, we find that selection effects play an important role for the interpretation of the TFR. In particular, galaxies selected via alternative methods cover lower-mass galaxies, and give rise to a steeper slope compared to luminosity selected galaxies.

The sample size and dynamical range of galaxy masses covered in various surveys play a critical role. While we find that the TFR relation extends at least out to $z \sim 3$, a smaller sample of 22 extreme emission line galaxies at $1.4 < z < 2.3$ reveals no clear relation (Maseda et al. 2014), while Cortese et al. (2014) find that low-mass galaxies ($\log M_*/\mathrm{M}_\odot < 10$) have roughly the same velocity dispersion of 20–30 km s^{-1}. A sample of ∼50 luminosity selected galaxies at $z \sim 2$ suggested a correlation (Förster Schreiber et al. 2009), and Erb et al. (2006b) find a correlation significance of 3.6σ in a similar sample size. In our larger combined sample we see a clear trend that the TFR extends to lower velocity dispersion in the $z < 2$ samples.

6.2 Evolution with redshift

For the galaxies compiled in this study we find no significant changes of the linear scaling between $\log M_*$ and $\log S_{0.5}$ with redshift out to $z \sim 3$. Figures 2 and 3 illustrate that the slope

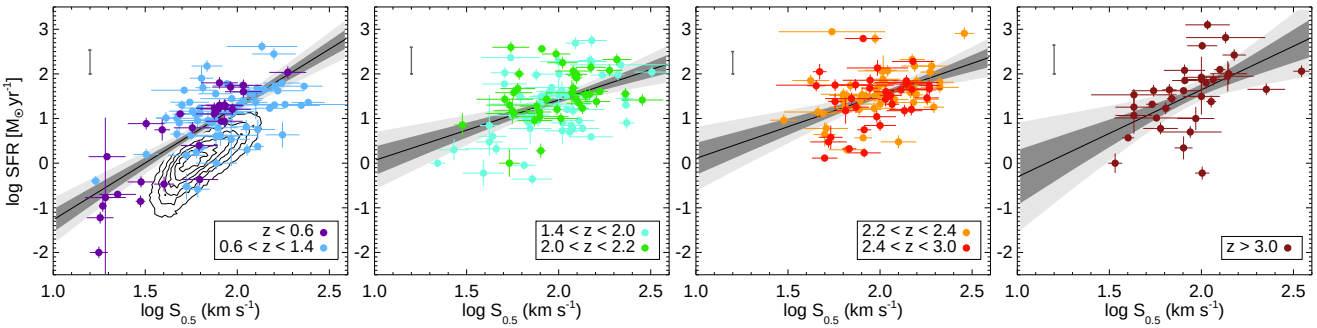

Figure 5. SFR versus $S_{0.5}$ divided into redshift intervals. Uncertainties for the measured SFRs are typically smaller than the symbol sizes. The background contours in the left panel represent star-forming SDSS galaxies at $z \sim 0$–0.4, which are clearly offset relative to the other galaxies. The scatter in each panel is represented by the bar in the upper left corner.

remains constant to within 1σ uncertainties, while the scatter increases significantly at $z > 3$. The only difference in slopes arises from sample selection as explained above. We find the slope and normalisation for the low-luminosity sample low-redshift bin to be consistent with that determined for $z \sim 1$ galaxies (Kassin et al. 2007). The (linear) fit to SDSS galaxies suggests a shift in the normalisation of 0.31 ± 0.15 dex from $z \sim 0$ to the low-luminosity sample at $z < 1.4$, suggesting a minor redshift evolution, although with the large uncertainties, it is also consistent with being constant to within a 2σ level.

Previous investigations that extend the TFR to higher redshifts find a shift of 1 dex at $z \sim 3$ (Gnerucci et al. 2011), and Cresci et al. (2009) find that the normalisation changes downwards by 0.4 dex for a sample of 18 galaxies at $z \sim 2$ compared to the local relation. Other studies find that the $S_{0.5}$ relation shows no evolution with redshift at $z < 1.2$ (Kassin et al. 2007), and while Kassin et al. (2012) find that it appears to be constant out to $z > 3$, they suggest that the reason is that the selection is biased towards higher mass galaxies.

Numerical simulations from EAGLE (Schaye et al. 2015) and semi-analytical models (Dutton et al. 2011) were used to investigate the redshift evolution of the classic TFR (Tiley et al. 2016). These models suggest a redshift evolution with a shift of about –0.2 dex from $z = 0$ to $z = 1.5$. This shift is consistent with the normalisation change from SDSS to our lowest redshift (low-luminosity) bin. The models suggest a further shift of –0.3 dex from $z = 1.5$ to $z = 3$, while the normalisations for this redshift interval listed in Table 1 imply a change of $+0.12 \pm 0.08$ for all galaxies, or -0.16 ± 0.29 for the low-redshift sample. Given the large uncertainties and the scatter of the data points, we cannot rule out any models based on our measurements.

When comparing the slopes and normalisations with previous studies, it is important to bear in mind that we include all measurement uncertainties and explore the relation over a larger dynamical range in stellar mass and redshift interval. The choice of method for fitting a straight line to the relation can also lead to different results (see Hogg et al. 2010). Choosing instead a simple linear regression or a bisector fit which does not include either individual measurement uncertainties or an intrinsic scatter term, gives steeper slopes for all redshifts and all subsamples, and is consistent with those previously reported ($A \sim 3.5$), i.e., a slope that large resembles the classical TFR or the local Faber–Jackson relations slope of 4 (Faber & Jackson 1976).

6.3 Scatter of the relations

Fitting linear relations (in log space), we find an intrinsic scatter of all the subsamples in the range 0.2–0.6 dex with a larger scatter in the low-luminosity sample compared to the high-luminosity sample. In the $z > 3$ bin the scatter is so high that the existence of a relation is not evident.

The scatter we derive is similar to a scatter of 0.47 dex for galaxies at $0.1 < z < 1.2$ (Kassin et al. 2007), 0.45 dex reported in (Vergani et al. 2012), and ∼0.3 dex in M_* for a local galaxy sample (Cortese et al. 2014). A smaller scatter of 0.14 dex in $\Delta \log \sigma$, equivalent to 0.29 dex in $\log M_*$, has been found for compact, massive star-forming galaxies at $z \sim 2.3$ (Barro et al. 2014), with a selection that only covers a range of 1 dex in stellar mass. The corresponding slope of 2.04 is similar to what we find in the same redshift bin $2.2 < z < 3$ for the combined sample.

The rather large scatter we find is a natural consequence of not restricting our sample to galaxies that are kinematically or morphologically similar. Studies of galaxies at $z = 0.6 - 1.2$ have revealed a roughly three-way split between rotating disks, merger-dominated galaxies and dispersion-dominated ones. By selecting only rotation dominated disks, the TFR scatter decreases significantly (Puech et al. 2008; Vergani et al. 2012).

6.4 Intepretations of a break in the TFR

We find that the M_*–$S_{0.5}$ slope depends on the luminosity range considered suggesting a non-linear relation (in log space). A similar non-linear relation is also seen in low-redshift star-forming SDSS galaxies. Fitting the data to a phenomenological model consisting of a low-luminosity power-law saturating at a high-mass asymptotic limit (Sect. 4.1) we find that the asymptotic mass limit of local SDSS galaxies is very similar to the high-redshift sample, with a turnover value of $\log S_{0.5,\mathrm{TO}} \sim 2.0 - 2.2$ depending on the chosen resolution limit and potential aperture losses. When studying the stellar mass TFR, Cortese et al. (2014) also find a non-linear behaviour, and note that the $S_{0.5}$ relation becomes steeper below $M_* = 10^{10} M_\odot$.

Several effects could give rise to a break in the relation. Velocity dispersion measurements are frequently used to compute the total dynamical mass of early-type galaxies, and since both quiescent and star-forming galaxies at low- and high redshifts follow a single TFR (Cortese et al. 2014; Barro et al. 2014), velocity dispersions measured from emission lines also trace the gravitational potential of a galaxy. However, in gas-rich late-type galaxies, the

gaseous component may contribute with a significant amount of mass, and therefore the total baryonic mass including stars and gas should be measured.

McGaugh et al. (2000) find a turnover in the $M_* - S_{0.5}$ relation with a steeper low-mass slope, but also determine an increasingly large gaseous component in low-mass galaxies. Without including the additional gas-mass the TFR becomes steeper in the low-mass end. Another example of a change in slope comes from Lyα emitting galaxies at $2 < z < 3$, which contain a larger gas-to-stellar mass fraction relative to other galaxy types (Rhoads et al. 2014). These galaxies lie systematically below the stellar-mass TFR in Kassin et al. (2007), but their dynamical masses show better agreement with the relation. Zaritsky et al. (2014) find a turnover at a rotational velocity at $\log v_c \approx 2$ for low-redshift galaxies in the classical TFR, and argue that the break can be corrected for when including gas masses in the baryonic TFR. Specifically, they find that including a constant fraction of halo-mass to baryonic mass of 7% will give rise to a linear TFR. If the galaxies investigated here were to follow this constant halo-baryon fraction, the amount of missing gas-mass in the lowest mass galaxies ($M_* \approx 10^{8-9}$ $M_\odot$), would be a factor of 20–10. While the amount of gas present in these star-forming galaxies may be significant compared to their stellar masses, such a high factor is larger than inferred for low-mass galaxies ($M_* < 10^{10}$ $M_\odot$) at $z \sim 1$, which have gas masses of a factor of $\sim$2 larger than their stellar masses (Stott et al. 2016). While some galaxies, particularly at $z > 3$, lie significantly below the $z \sim 1$ stellar-mass TFR, most galaxies exhibit a spread around the relation with objects both above and below the relation. Hence, an increased gas fraction in high redshift galaxies cannot be the only explanation of a turnover.

Another effect that could change the slope primarily at the high-mass end is the turbulent motion related to star-formation activity either from in- or outflows, shocks or merger activities. Turbulent motions increase the velocity dispersion and give rise to a flatter relation. As star-formation activity increases by a factor of $\sim$10 from $z = 0$ to $z > 1$, this would imply a stronger effect in a higher redshift sample. However, there are indications that star-formation activity does not significantly alter the location of galaxies in the TFR. Galaxies of any Hubble types appear to follow the same mass-$S_{0.5}$ relation (Cortese et al. 2014) and compact quiescent massive galaxies appear to follow the same relation as their star-forming counterparts (Barro et al. 2014). In our samples, the slope of the $S_{0.5}$-SFR relation becomes flatter with redshift which could be interpreted as a dynamical effect in the high-mass end. As a very high SFR influences a low-mass galaxy more, the specific SFR (i.e. SFR/M_*) better probes the impact of the star formation activity on the velocity dispersions. In our sample there are no clear correlations between the specific SFR and $S_{0.5}$ for any of the subsamples in any of the redshift bins.

High-redshift galaxies are increasingly dispersion dominated (e.g. Förster Schreiber et al. 2009), and galaxies exhibit more ordered rotation with decreasing redshifts (Kassin et al. 2012). At $z < 1$ Kassin et al. (2012) find a threshold at $\log M_* = 10.4$ where galaxies transition from low-mass disordered to more ordered kinematics. At any redshift, the most massive star-forming galaxies are the ones that have rotationally supported disks, and this transition progresses to lower masses with cosmic time. Including a high rotational velocity component in addition to the measured velocity dispersion in the calculation of $S_{0.5}$ causes galaxies to deviate from a steep $\sigma - M_*$ relation, and will give rise to a flattening of the $S_{0.5} - M_*$ relation in the high-mass end. The down-sizing of galaxies with increasing rotational support with decreasing redshift implies a change in the turnover point to lower stellar masses and lower velocity dispersions. This is further suggested by the observed change in the turnover point between the SDSS and the higher redshift sample.

To summarise, the likely explanations for a turnover in the TFR, is either a higher gas-mass fraction in low-mass galaxies, or a higher dark matter to stellar mass fraction. Based on the arguments above, and that the halo-models appear to broadly describe the observations in section 4.2, it seems that the dark-matter contribution to the break is a valid interpretation, while a vertical shift in Fig. 4 can be explained by a change in the gas fraction. Future observations of total gas masses in high redshift galaxies are needed for a conclusion of the dominant effect.

7 SUMMARY

By examining a variety of galaxy samples out to $z \sim 5$, covering a wide dynamical range in stellar masses, we find a redshift invariant TFR between stellar mass and the kinematic estimator $S_{0.5}$ that combines velocity dispersion and galaxy rotations derived from emission lines. While there is no strong evidence for evolution out to $z \sim 3$, we find that sample definition and fitting methods play a crucial role in the determined slopes and normalisations of the fits to the TFR. This conclusion also holds when we extend the study to low-redshift star-forming galaxies in the SDSS. Between $z = 0$ and $z = 2$, the SFR–$S_{0.5}$ relation displays a redshift evolution similar to the M_*–SFR relation, also known as the main sequence for star-forming galaxies, suggesting that these redshift changes arise from the same underlying physical evolution mechanism.

We find that the stellar mass TFR is not linear and has a steeper slope at the low-mass end. The reason for a turnover can be caused by a several physical effects. A large fraction of baryons in star-forming dwarf galaxies is in gaseous form, and adding this component to the stellar mass is found to create a linear relation over the whole dynamical range. One would expect a linear relation in log space as the global velocity dispersion traces the dynamical mass of the galaxy. In this study we have not investigated dynamical masses because the galaxies radii are not measured for the majority of the sample. Instead, we rely on the stellar mass alone which may not be representative for the dynamics in the galaxy.

A larger rotation causes an increase in $S_{0.5}$ for more massive galaxies and at lower redshifts when galaxy disks settle into more ordered rotations. Since galaxies have more ordered rotation with increased stellar mass and increased cosmic time, this would imply a shift of the turnover towards lower values at lower redshifts.

A higher fraction of dark matter in low-mass galaxies also causes a turnover of the relation and results in a steeper slope at the low-mass end. The break we infer from the observations broadly agree with halo ocupation distribution models, which are derived by matching modelled halo masses with observed galaxy stellar masses, and not the galaxies' total baryonic masses (Guo et al. 2010; Behroozi et al. 2013; Moster et al. 2013). We find a good agreement at low redshifts, but at $z \sim 2$, the observations suggest a less pronounced break compared to model predictions. At the high mass end, the observed galaxies have a lower stellar mass than predicted, which can be explained by a higher gas fraction and consequently a lower stellar mass fraction. Models that include gas consumption and conversion into stars are better able to reproduce the normalisation of the TFR. At the low-stellar mass end, the observations appear to have a too high stellar mass compared to the models. However, the slope at the low-mass end, depends on rela-

tively few (only 20 galaxies with $\log S_{0.5} < 1.6$) low-mass, high redshift galaxies. Further studies to explore the low-mass end of high-redshift galaxy dynamics are needed to securely constrain the low-mass end slope of the TFR relation.

ACKNOWLEDGEMENTS

LC acknowledges support from an YDUN grant DFF 4090-00079. This research has made use of the GHostS database (`www.grbhosts.org`), which is partly funded by Spitzer/NASA grant RSA Agreement No. 1287913. We thank James Rhoads, Anja von der Linden, Arianna Di Cintio and Chris Brook for useful discussions. We also thank the referees for insightful comments to the manuscript.

REFERENCES

Baldwin, J. A., Phillips, M. M., & Terlevich, R. 1981, PASP, 93, 5
Barro, G., et al. 2014, ApJ, 795, 145
Behroozi, P. S., Wechsler, R. H., & Conroy, C. 2013, ApJ, 770, 57
Bell, E. F., & de Jong, R. S. 2001, ApJ, 550, 212
Belli, S., Jones, T., Ellis, R. S., & Richard, J. 2013, ApJ, 772, 141
Bian, F., et al. 2010, ApJ, 725, 1877
Brinchmann, J., Charlot, S., White, S. D. M., Tremonti, C., Kauffmann, G., Heckman, T., & Brinkmann, J. 2004, MNRAS, 351, 1151
Brook, C. B., Di Cintio, A., Knebe, A., Gottlöber, S., Hoffman, Y., Yepes, G., & Garrison-Kimmel, S. 2014, ApJ, 784, L14
Bryan, G. L., & Norman, M. L. 1998, ApJ, 495, 80
Chabrier, G. 2003, PASP, 115, 763
Chen, X.-Y., Hao, C.-N., & Wang, J. 2008, ChJAA, 8, 25
Christensen, L., D'Odorico, S., Pettini, M., Belokurov, V., Evans, N. W., Kellogg, M., & Vernet, J. 2010, MNRAS, 406, 2616
Christensen, L., et al. 2012a, MNRAS, 427, 1973
Christensen, L., et al. 2012b, MNRAS, 427, 1953
Christensen, L., Vreeswijk, P. M., Sollerman, J., Thöne, C. C., Le Floc'h, E., & Wiersema, K. 2008, A&A, 490, 45
Conselice, C. J., Bundy, K., Ellis, R. S., Brichmann, J., Vogt, N. P., & Phillips, A. C. 2005, ApJ, 628, 160
Contini, T., et al. 2012, A&A, 539, A91
Cortese, L., et al. 2014, ApJ, 795, L37
Cresci, G., et al. 2009, ApJ, 697, 115
Daddi, E., et al. 2007, ApJ, 670, 156
de Ugarte Postigo, A., et al. 2013, A&A, 557, L18
de Ugarte Postigo, A., et al. 2014, A&A, 563, A62
Dutton, A. A., et al. 2011, MNRAS, 410, 1660
Elliott, J., et al. 2013, A&A, 556, A23
Epinat, B., et al. 2012, A&A, 539, A92
Erb, D. K., Steidel, C. C., Shapley, A. E., Pettini, M., Reddy, N. A., & Adelberger, K. L. 2006a, ApJ, 647, 128
Erb, D. K., Steidel, C. C., Shapley, A. E., Pettini, M., Reddy, N. A., & Adelberger, K. L. 2006b, ApJ, 646, 107
Faber, S. M., & Jackson, R. E. 1976, ApJ, 204, 668
Flores, H., Hammer, F., Puech, M., Amram, P., & Balkowski, C. 2006, A&A, 455, 107
Förster Schreiber, N. M., et al. 2009, ApJ, 706, 1364
Frederiksen, T. F., Graur, O., Hjorth, J., Maoz, D., & Poznanski, D. 2014, A&A, 563, A140
Frederiksen, T. F., Hjorth, J., Maund, J. R., Rodney, S. A., Riess, A. G., Dahlen, T., & Mobasher, B. 2012, ApJ, 760, 125
Fynbo, J. P. U., et al. 2013, MNRAS, 436, 361
Fynbo, J. P. U., et al. 2014, A&A, 572, A12
García-Lorenzo, B., et al. 2015, A&A, 573, A59
Genzel, R., et al. 2006, Nature, 442, 786
Gerssen, J., Wilman, D. J., & Christensen, L. 2012, MNRAS, 420, 197
Glazebrook, K. 2013, PASA, 30, 56
Gnerucci, A., et al. 2011, A&A, 528, A88
Gonçalves, T. S., et al. 2010, ApJ, 724, 1373
Guo, Q., White, S., Li, C., & Boylan-Kolchin, M. 2010, MNRAS, 404, 1111
Guseva, N. G., Izotov, Y. I., Fricke, K. J., & Henkel, C. 2011, A&A, 534, A84
Hainline, K. N., Shapley, A. E., Kornei, K. A., Pettini, M., Buckley-Geer, E., Allam, S. S., & Tucker, D. L. 2009, ApJ, 701, 52
Hjorth, J., et al. 2012, ApJ, 756, 187
Hjorth, J., et al. 2005, Nature, 437, 859
Hogg, D. W., Bovy, J., & Lang, D. 2010, ArXiv e-prints 1008.4686
Jaunsen, A. O., et al. 2008, ApJ, 681, 453
Jones, T., Ellis, R. S., Richard, J., & Jullo, E. 2013, ApJ, 765, 48
Jones, T. A., Swinbank, A. M., Ellis, R. S., Richard, J., & Stark, D. P. 2010, MNRAS, 404, 1247
Kassin, S. A., et al. 2012, ApJ, 758, 106
Kassin, S. A., et al. 2007, ApJ, 660, L35
Kelly, B. C. 2007, ApJ, 665, 1489
Kewley, L. J., Jansen, R. A., & Geller, M. J. 2005, PASP, 117, 227
Krogager, J.-K., et al. 2013, MNRAS, 433, 3091
Krühler, T., et al. 2012, A&A, 546, A8
Krühler, T., et al. 2011, A&A, 534, A108
Krühler, T., et al. 2015, A&A, 581, A125
Kulas, K. R., et al. 2013, ApJ, 774, 130
Law, D. R., Steidel, C. C., Erb, D. K., Larkin, J. E., Pettini, M., Shapley, A. E., & Wright, S. A. 2009, ApJ, 697, 2057
Lehnert, M. D., Le Tiran, L., Nesvadba, N. P. H., van Driel, W., Boulanger, F., & Di Matteo, P. 2013, A&A, 555, A72
Leloudas, G., et al. 2015, MNRAS, 449, 917
Lemoine-Busserolle, M., Bunker, A., Lamareille, F., & Kissler-Patig, M. 2010, MNRAS, 401, 1657
Lemoine-Busserolle, M., & Lamareille, F. 2010, MNRAS, 402, 2291
Levesque, E. M., et al. 2010, MNRAS, 401, 963
Maseda, M. V., et al. 2013, ApJ, 778, L22
Maseda, M. V., et al. 2014, ApJ, 791, 17
McGaugh, S. S., Schombert, J. M., Bothun, G. D., & de Blok, W. J. G. 2000, ApJ, 533, L99
Melnick, J., Terlevich, R., & Terlevich, E. 2000, MNRAS, 311, 629
Miller, S. H., Bundy, K., Sullivan, M., Ellis, R. S., & Treu, T. 2011, ApJ, 741, 115
Miller, S. H., Ellis, R. S., Sullivan, M., Bundy, K., Newman, A. B., & Treu, T. 2012, ApJ, 753, 74
Milvang-Jensen, B., Aragón-Salamanca, A., Hau, G. K. T., Jørgensen, I., & Hjorth, J. 2003, MNRAS, 339, L1
Mitchell, P. D., Lacey, C. G., Baugh, C. M., & Cole, S. 2016, MNRAS, 456, 1459
Moster, B. P., Naab, T., & White, S. D. M. 2013, MNRAS, 428, 3121

Noeske, K. G., et al. 2007, ApJ, 660, L43
Pérez-Montero, E., et al. 2009, A&A, 495, 73
Perley, D. A., et al. 2008, ApJ, 672, 449
Perley, D. A., et al. 2013, ApJ, 778, 128
Péroux, C., Bouché, N., Kulkarni, V. P., York, D. G., & Vladilo, G. 2011, MNRAS, 410, 2251
Pettini, M., et al. 2010, MNRAS, 402, 2335
Pettini, M., Shapley, A. E., Steidel, C. C., Cuby, J.-G., Dickinson, M., Moorwood, A. F. M., Adelberger, K. L., & Giavalisco, M. 2001, ApJ, 554, 981
Posti, L., Nipoti, C., Stiavelli, M., & Ciotti, L. 2014, MNRAS, 440, 610
Press, W. H., Teukolsky, S. A., Vetterling, W. T., & Flannery, B. P. 1992, Numerical recipes in FORTRAN. The art of scientific computing
Puech, M., et al. 2008, A&A, 484, 173
Queyrel, J., et al. 2012, A&A, 539, A93
Rhoads, J. E., Malhotra, S., Richardson, M. L. A., Finkelstein, S. L., Fynbo, J. P. U., McLinden, E. M., & Tilvi, V. S. 2014, ApJ, 780, 20
Richard, J., Jones, T., Ellis, R., Stark, D. P., Livermore, R., & Swinbank, M. 2011, MNRAS, 126
Salpeter, E. E. 1955, ApJ, 121, 161
Savaglio, S., Glazebrook, K., & Le Borgne, D. 2009, ApJ, 691, 182
Schaye, J., et al. 2015, MNRAS, 446, 521
Schulze, S., et al. 2014, A&A, 566, A102
Shapley, A. E., Erb, D. K., Pettini, M., Steidel, C. C., & Adelberger, K. L. 2004, ApJ, 612, 108
Siana, B., Teplitz, H. I., Chary, R., Colbert, J., & Frayer, D. T. 2008, ApJ, 689, 59
Steidel, C. C., et al. 2014, ApJ, 795, 165
Stott, J. P., et al. 2016, MNRAS, 457, 1888
Svensson, K. M., et al. 2012, MNRAS, 421, 25
Swinbank, A. M., Sobral, D., Smail, I., Geach, J. E., Best, P. N., McCarthy, I. G., Crain, R. A., & Theuns, T. 2012, MNRAS, 426, 935
Swinbank, A. M., et al. 2009, MNRAS, 400, 1121
Teplitz, H. I., et al. 2000, ApJ, 533, L65
Thomas, D., et al. 2013, MNRAS, 431, 1383
Thöne, C. C., et al. 2011, MNRAS, 414, 479
Thöne, C. C., et al. 2008, ApJ, 676, 1151
Thöne, C. C., Greiner, J., Savaglio, S., & Jehin, E. 2007, ApJ, 671, 628
Tiley, A. L., et al. 2016, MNRAS, 460, 103
Tremonti, C. A., et al. 2004, ApJ, 613, 898
Trujillo-Gomez, S., Klypin, A., Primack, J., & Romanowsky, A. J. 2011, ApJ, 742, 16
Tully, R. B., & Fisher, J. R. 1977, A&A, 54, 661
Vergani, D., et al. 2012, A&A, 546, A118
Vergani, S. D., et al. 2011, A&A, 535, A127
Weiner, B. J., et al. 2006, ApJ, 653, 1027
Whitaker, K. E., et al. 2014, ApJ, 795, 104
Wiersema, K., et al. 2007, A&A, 464, 529
Williams, M. J., Bureau, M., & Cappellari, M. 2010, MNRAS, 409, 1330
Wisnioski, E., et al. 2015, ApJ, 799, 209
Wisnioski, E., Glazebrook, K., Blake, C., Poole, G. B., Green, A. W., Wyder, T., & Martin, C. 2012, MNRAS, 422, 3339
Wright, S. A., Larkin, J. E., Law, D. R., Steidel, C. C., Shapley, A. E., & Erb, D. K. 2009, ApJ, 699, 421

GRB name	z	log M^{*} [a] [$M_{\odot}$]	σ [km s^{-1}]	SFR [M$_{\odot}$ yr^{-1}]	ref
GRB980425	0.0085	9.20±0.07	22.4±0.2	0.2	[1]
GRB000210	0.8460	9.31±0.08	64±5	2.28	[25]
GRB000418	1.1181	9.26±0.14	41±5	10.4	[25]
GRB000911	1.0578	9.32±0.26	32±6	1.57	[25]
GRB011211	2.1433	9.77±0.47	37.5±15.5	4.9	[26]
GRB021004	2.3299	9.31±0.08	68.8±11.0	2.28	[26]
GRB031203	0.1055	8.84±0.43	49.0±3.0	12.7	[2]
GRB030329	0.1680	7.75±0.15	18.6±0.9	0.2	[3]
GRB050416	0.6540	9.84±0.74	47±4	1.5±0.2	[4,24]
GRB050709	0.1606	8.66±0.07	29.8±1.8	0.14	[21,26]
GRB050915A	2.5272	10.56±0.15	96.8±37.1	136±55	[12,20]
GRB051022	0.8061	10.42±0.18	88±5	60	[24]
GRB060218	0.0335	7.78±0.08	18.0±3.0	0.06	[5]
GRB060505	0.0889	9.41±0.01	62.5±1.5	0.43	[6]
GRB060614	0.1250	7.95±0.13	17.7±2.0	0.01	[7,26]
GRB060719	1.5318	10.11±0.15	42±5	7±11	[12,20,24]
GRB060814	1.9229	9.99±0.05	54.9±20.3	232±37	[12,20]
GRB061126	1.1588	10.62±0.24	129.0±10.0	2.38	[8]
GRB070306	1.4959	10.4±0.2	133.0±10.0	34±29	[9,10]
GRB070802	2.4538	9.7±0.2	63.6±29.4	10±18	[4,10]
GRB071021	2.4513	11.08±0.03	151.5±39.7	190±23	[12,20]
GRB080207	2.0858	11.25±0.11	167.5±16.5	40.7±1.6	[4,11]
GRB080605	1.6403	9.90±0.10	62.0±4.0	31.0±10	[4,10]
GRB080805	1.505	9.7±0.2	70.0±18.5	6±5	[10,12]
GRB081109	0.9787	9.82±0.09	77.2±7.8	13±4	[10]
GRB090323	3.5832	11.2±0.75	60.±13	6	[24]
GRB090407	1.4474	10.18±0.15	80.2±25.2	28.1±12.2	[10,12]
GRB090426	2.609	10.35±0.06	52.5±12	3	[13,14]
GRB090926B	1.2425	10.1±0.4	63.9±9.4	80±50	[10]
GRB091127	0.4903	8.70±0.20	60.0±10.0	0.22	[15]
GRB100418	0.6239	9.28±0.28	56±4	4.2±0.9	[24]
GRB100621A	0.5420	8.98±0.14	82±4	8.7±0.8	[10,24]
GRB110918A	0.984	10.68±0.16	126±18	23±20	[16]
GRB120119	1.7280	9.30	104±17	43±19	[24]
GRB120422A	0.2826	8.95±0.04	19.6±0.2	0.3±0.3	[22]
GRB120624B	2.1974	10.6±0.3	123.0±11.0	91±6.	[17]
GRB130427	0.3399	9.0±0.2	40.0±5.0	0.34±0.13	[18,24]
GRB130603B	0.3565	9.8±0.2	39.1±3.8	5.6±3.1	[19]
GRB140506A	0.8893	9.0	61±9	0.26±0.11	[23,24]

Table A1. GRB host data. [a] Stellar masses are adopted from the GHostS compilation in Savaglio et al. (2009). References.– [1] Christensen et al. (2008), [2] Guseva et al. (2011), [3] Thöne et al. (2007), [4] Hjorth et al. (2012), [5] Wiersema et al. (2007), [6] Thöne et al. (2008), Thöne et al. in prep. [7] Hjorth et al. (2005), [8] Perley et al. (2008), [9] Jaunsen et al. (2008), [10] Krühler et al. (2011), [11] Svensson et al. (2012), [12] Krühler et al. (2012), [13] Thöne et al. (2011), [14] Levesque et al. (2010), [15] Vergani et al. (2011), [16] Elliott et al. (2013), [17] de Ugarte Postigo et al. (2013), [18] Xu et al. (2013), [19] de Ugarte Postigo et al. (2014), [20] Perley et al. (2013), [21] Hjorth et al. (2005), [22] Schulze et al. (2014), [23] Fynbo et al. (2014), [24] Krühler et al. (2015), [25] T. Krühler, priv. comm., [26] ESO xshooter archive, this paper.

Wuyts, E., Rigby, J. R., Gladders, M. D., Gilbank, D. G., Sharon, K., Gralla, M. B., & Bayliss, M. B. 2012a, ApJ, 745, 86
Wuyts, E., Rigby, J. R., Sharon, K., & Gladders, M. D. 2012b, ApJ, 755, 73
Xu, D., et al. 2013, ApJ, 776, 98
Yuan, T.-T., Kewley, L. J., Swinbank, A. M., & Richard, J. 2012, ApJ, 759, 66
Zaritsky, D., et al. 2014, AJ, 147, 134